RSC Advances

ROYAL SOCIETY
OF CHEMISTRY

www.rsc.org/advances

Table of Content:

Spontaneous hyper-branching in ZnO nanostructures: morphology dependent electron emission and light detection

Shreyasi Pal[a], Soumen Maiti[a], Uday Narayan Maiti[b], and Kalyan Kumar Chattopadhyay[a]*

[a]Thin Films and Nanoscience Laboratory, Department of Physics, Jadavpur University, Kolkata 700032, India, [b]Indian Institute Technology, Guwahati, India

Corresponding Author: Email: kalyan_chattopadhyay@yahoo.com
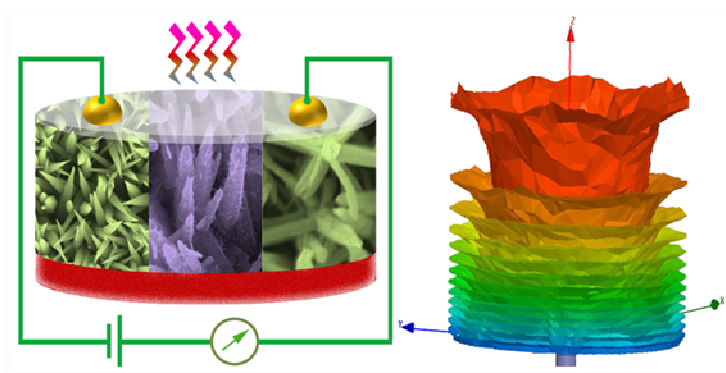
Structure and intrinsic defect induced electron field emission and photodetection are monitored in ZnO nanoforms with assorted morphology prepared at complete ambient condition via facile wet chemical approach.

Spontaneous hyper-branching in ZnO nanostructures: morphology dependent electron emission and light detection

Shreyasi Pal[a], Soumen Maiti[a], Uday Narayan Maiti[b], and Kalyan Kumar Chattopadhyay[a]*

[a]Thin Films and Nanoscience Laboratory, Department of Physics, Jadavpur University, Kolkata 700032, India, [b]Department of Physics, Indian Institute Technology, Guwahati, India

Corresponding Author: Email: kalyan_chattopadhyay@yahoo.com

Abstract:

Unprecedented proficiencies of higher dimensional ZnO nanoforms over their low dimensional counterpart in emerging technologies motivated the researchers to design ZnO hierarchical architectures which are expected to upsurge their performances to device benchmarks. Starting from 1D ZnO nanospike array, hierarchical cactus and tree like ZnO arrays with increasing branching and complexities have been grown via simple wet chemical approach at complete ambient condition. Zero thermal budget, large area fabrication and absence of any structure-directing agents are the novel highlights of current synthesis protocol. Cathodoluminescence spectroscopic investigation reveals gradual increment in defect constitution in these nanoforms with the increase of structural complexity. The synthesized nanostructure arrays display promises in electron field emission owing to their structural uniqueness as indicated by field distribution calculation using ANSYS electromagnetic software. Furthermore, these higher order nanostructures are capable of detecting UV light with a photocurrent gains as high as 2.21×10^4.

Introduction:

Geometrically intricate multiscale hierarchical configurations embrace with one dimensional (1D) nanostructural building blocks by inheriting the intrinsic features of nanoscale singularities as well as exhibiting highly activated surface area and robust stability providing by two or higher level structures, draw a paramount significance from material chemists and technologists.[1-3] Among these higher dimensional superstructures, dendritic and complex branched nano-architectures are of special significance owing to upsurge of connection points into them which in turn offer resources for parallel association and interconnection of functional components.[4-6] Additionally, high degrees of complexity associated with these nanoforms provide a broad application window in catalysis,[7,8] photodetection,[9] sensing,[10] optoelectronics,[11] field electron emission,[12-15] photovoltaic devices[16] and etc. ZnO, with its vast morphological assortments, is possibly the most explored metal oxide in this respect owing to the several intriguing features like nontoxicity, biocompatibility, chemical and photochemical stability, electrochemical activities possession etc., relying on which, these interesting hierarchies represent their propitious position to be the main structural unit for several optoelectronic and electronic devices fabrication.[17-23] Amalgamation of the nanoscale building blocks into these complicated complexions is generally attained via oriented aggregation, self-assembly, templating synthesis, sequential seeding and growth etc.; where the adopted experimental pathways are hydrothermal, electro-deposition, physical vapor deposition, chemical vapor deposition (CVD), metalorganic CVD, wet chemical routes etc.[24-32] Among these enlisted practices, low temperature solution processed route is most suitable for the creation of combinatorial architectures owing to several expedient features like nominal thermal budget, straightforward processing, easy fabrication etc.; whereas the others are not only expensive, but also require several stringent criteria and complex

manipulations.[7,33-34] Considering all the aforesaid particularities, novel, effective and facile wet chemical routes for the fabrication of ZnO hierarchical nanostructures are highly desirable.

Going beyond the often used multistep seeding and growth protocols to achieve higher dimensional nanoform,[31,35] ZnO branch hierarchy have been realized in facile manner where the nucleation for secondary evolution and subsequent growth taken place in same reaction. Unrestricted by any stringent criteria such as sequential seeding or necessity of high temperature; this completely ambient conditioned protocol can yield large area thin film, thus highlighting its accessibility and simplicity over other reported methods. Compactness as well as the dimension of secondary branches in the nanostructure, a key parameter for their practical usage, can be tailored in subtle fashion by manipulating the zinc salt concentration only. As an immediate application of these morphology tuned hierarchies, field emitters and UV photo-detectors were fabricated using them which outperform the same constructed with 1-D nanostructures, a de facto choice till date. In addition to the morphology, intrinsic variation of the defect structures of these as synthesized nanoforms are also found to influence the field electron emission as well as the photoresponse characteristics. Being not restricted to electron emission or photodetection applications; these ZnO hierarchical architectures with nano-branches and self-assembled junctions are also appealing for other possible usage such as in sensors, solar cells, photocatalyst and so forth.

Experimental:

Deposition of the nanospike and hierarchical nanoarchitectures was executed both on glass and ITO coated glass substrate. For nanospike synthesis two separately prepared 10 mL solution of 2M potassium hydroxide (KOH) and 0.25 M zinc nitrate hexahydrate ($Zn(NO_3)_2$, $6H_2O$) were mixed together and transferred to a 30 mL borosilicate glass bottle. Thereafter, one analytical

grade zinc foil (1cm$\times$1cm$\times$1μm) rubbed with fine emery paper along with a KMnO$_4$ activated substrate (glass and ITO coated glass) was placed in the bottle and kept for 3 h at complete ambient condition. Finally, the substrate was washed with ample amount of D.I. water and dried at room temperature.

Now, for realization of nanospike based hierarchical architectures, the pre-synthesized nanospike coated sample was used as substrate further. The experimental condition followed in these cases was nearly similar to previous except the zinc salt and potassium hydroxide concentration. Separate set of experiments were performed by varying the amount of zinc salt keeping the KOH concentration fixed. Subsequent treatment with 0.13 M zinc nitrate and 1 M KOH ensued nominal geometrical complex structure formation over nanospike whereas reaction with unvaried KOH amount, only higher zinc salt concentration (0.18 M) than previous resulted more complex nanoform.

Characterization: Please see the supporting information†.

Results & Discussion:

Morphological & structural analysis:

Fig. 1a displays low magnification FESEM image and wafer scale synthesis (inset of Fig. 1a) of ZnO nanospikes. Zoomed observation (Fig. 1b) exposes that each individual nanospikes possess a smooth side surface and hexagonal building blocks, having average length ~1 μm and diameter ~100-200 nm from top to base. Ambient conditioned modification via successive wet chemical technique leads morphological changes of the pristine nanospikes and the corresponding microscopic images are manifested in Fig. 1[c,d]. In complete contrast to original nanospikes, tiny spines grow sparsely in radial direction over nanospikes backbone and formed "cactus" like morphology for low zinc salt concentration assisted modification reaction. These spines having

average diameter ~10 to 30 nm from tip to base and lengths ranging from 40-60 nm display epitaxial relationship with parent nanospikes (Fig. 1c). Instead of short sprouted spines, subsequent chemical treatment of the nanospikes with higher zinc salt concentration ensures the formation of nanostructured "pine tree" like robust branched network (Fig. 1d).

Similar with the cactus like hierarchy, here also secondary branches are generated in radial fashion over the hexagonal prismatic nanospike facets. However, converse to cactus formed hierarchy, higher dimensional aspects of the branches are found in this case as the average length as well as top-base diameters are increased to ~350 nm and ~25-75 nm respectively (Fig. 1d). Henceforth, we will denote the parent sample simply as nanospike and low and high zinc salt assisted modified hierarchical samples as nanocactus and nanotree respectively.

The TEM analysis of the samples reveals detail surface morphology and structural information of the as prepared ZnO nanostructures. Inset of Fig. 2a shows TEM image of a single ZnO nanospike having an average length ~ 500 nm with a lateral dimension ~10-70 nm at top to base. A precise observation depicts the smooth side surfaces of nanospikes where trace of other secondary growth is completely absent. High-resolution transmission electron microscopy (HRTEM) image of the nanospike (Fig. 2a) with distinct parallel lattice fringes indicate their well crystallinity where the interplanar spacing of 0.26 nm agrees well with the same of (001) plane of hexagonal wurtzite ZnO.[36] Further, the selected area diffraction (SAED) pattern comprising with bright circular spots, confirms their single crystalline nature (Fig. 2d). Several secondary branches radiating outwards with different dimensions found to appear over the pristine nanospikes to form the nanocactus and nanotree morphology which are evident from insets of Fig. 2[b,c]. For nanocactus, low dimensional blunt branch nanospikes over the primary nanospikes are evident from the TEM image (inset of Fig. 2b). Conversely for nanotree,

secondary outgrowths with higher dimensionality are also feasible from the corresponding TEM image (inset of Fig. 2c). In spite of their discernible dimensional differences, both secondary nanocactus and nanotree branches maintain high crystallinity and carry off the same functional material (ZnO) as manifested from corresponding HRTEM images and SAED patterns (Fig. 2[e,f] and their insets).

X-ray diffraction (XRD) pattern of the as synthesized samples with different geometrical complexity is presented in Fig. 3a. All peaks in the diffraction patterns can be well indexed with the hexagonal wurtzite phase of ZnO (JCPDS card no. 36-1451) with lattice constants of a =3.25 Å and c =5.21 Å. The absence of any other diffraction peaks conclusively excludes the possibility of impurity phases and indicates phase purity of the synthesized samples.

Along with XRD analysis, X-ray photoelectron spectroscopy (XPS) investigation of a reference sample (nanotree) was further executed to investigate the surface composition of products. Referencing the C1s spectra at 284.6 eV, all the binding energies were energy corrected. A typical asymmetric O1s spectrum corresponds to nanotree sample is shown in Fig. 3b which can be deconvoluted to three peaks. First and the most intense peak at binding energy ~529.7 eV is accredited to the normal wurtzite structure of zinc oxide [37] whereas the second one peaking at ~531.1 eV is related with O_2^- ion in the oxygen deficient region.[38] Further, peak at higher binding energy ~532.2 eV is associated with O_2^- of OH or H_2O species [39] which is almost inevitable with the chemically processed ZnO nanostructure irrespective of their state i.e. powder or thin film form.[40] Finally, Zn 2p spectrum in Fig. 3c with two highly intense peaks at 1022.5 and 1045.5 confirms the doublet formation and presences of Zn^{2+} only in the sample.[41] Finally, the presence of no other impurity related peaks in survey spectrum in Fig. 3d corroborates the XRD results.

Surface area, a vital structural parameter of nanostructure strongly depends on their morphology. As in our samples geometrical intricacy increases gradually there should be obvious variance in their surface area. Fig. 4[a-c] shows the nitrogen (N_2) physical adsorption-desorption isotherms for ZnO nanospike, hierarchical nanocactus and nanotree. The Brunauer-Emmett-Teller (BET) surface area of nanospike, nanocactus and nanotree are found to 34.461, 49.856 and 68.576 m^2/g respectively. Such results indicate enhanced N_2 adsorption of hierarchical nanostructures and maximum surface area for the nanotree sample.

Cathodoluminescence study:

Cathodoluminescence (CL) is an effective tool to probe the optical features of nanomaterials which also reveals the spatial distribution as well as the interconnection between the sample morphology and the luminescence.[42] Room temperature CL spectra of the synthesized ZnO nano-architectures recorded at an accelerating voltage of 1 kV is presented in Fig. 5a. CL spectra for nanospike, nanocactus and nanotree comprises of two characteristics peaks, one narrow peak in UV region around ~382 nm and a broad emission band centered around ~550 nm. The UV emission is accredited to near band edge transition of wide band gap ZnO,[43] while the visible emission is associated with different deep lying defects in ZnO, such as oxygen vacancies with different charge states, zinc vacancies and zinc interstitial etc. For facile comparison of their defect related emission all the UV peaks are normalized and presented in same figure. It is also confirmed that the visible emission peak around ~550 arises due to the presence of oxygen vacancy and intensity of the emission peak is associated with vacancy concentration; higher the vacancy concentration greater is the intensity of peak.[44] In the CL spectra, the intensity of defect related emission peak is remarkably increased gradually with growth of higher degree secondary branches where such enhancement is related to the degree of oxygen vacancies constitution. As

oxygen vacancy mainly resides on the nanostructure surfaces, the higher surface area nanoforms should correspond to the presence of higher amount of defects and should exhibit an enhancement in visible emission. Hierarchical nanotree comprising of dense and higher dimensional secondary branches possess high surface area as compared to nanocactus sample as the later consists of sparse distribution of low dimensional secondary branches. On the other hand, nanospike sample, devoid of any secondary branches, own very low surface area compared to the previous two (clear from BET surface area values). In this aspect, surface related defects concentration should follow the analogous order which is ultimately manifested in intensity variation of visible emission related peak.

Further, intensity increment of defect related emission peak with increase of secondary branches in hierarchical nanoforms is corroborated by their oxygen content ratio (determined from EDX measurement of individuals) (Fig. 5b) and corresponding elemental mapping (Fig.S1 in ESI†). With the growth of secondary branches, the atomic percentage ratio of zinc to oxygen increases from 1.05 (nanospike) to 1.24 (nanotree) which indicates oxygen deficiency in hierarchical sample and thereby opens up the possibility to constitute higher amount of defects.

The Raman spectra of the as grown ZnO nanostructures within the range from 90-600 cm^{-1} are shown in Fig.5c. All the spectra are dominated by two sharp peaks, one peaking at ~98 cm^{-1} and other at ~437 cm^{-1}. Among these, the first one is designated as E_2 (low) whereas the later labeled as E_2 (high);[43] also known as Raman active phonon mode which is the characteristic band of hexagonal wurtzite phase ZnO. On the other hand, weaker peaks at ~332 cm^{-1} and ~389 cm^{-1} are related to E_{2H}–E_{2L} and A_1(TO) modes respectively.[45] Raman signals are very sensitive to the crystal quality as well as the defect structure of the nanostructure.[46] Very close inspection of these spectra discloses that, with the increase of hierarchy in the nanoforms, the intensity of

the Raman active mode at 437 cm^{-1} gradually decreases. Such decrement in the intensity of Raman signal is connected with the presence of defects in the nanoforms. Increase in geometrical complexity and thereby upsurge in the surface area nanoforms raises the defect constitutions (evident from the CL spectra). As a consequence of enhanced defect constitution, minimum intensity of the above mentioned Raman peak is observed in nanotree sample and vice versa in nanospike sample.[46] Such results confirm that the changes in the defect constitution in the as prepared samples originate from structural modifications and substantiate the CL results.

Plausible Growth Mechanism:

The nanostructured samples fabrication procedure is schematically illustrated in Figure 6. Based on the aforesaid structural evolution of the nanoforms, a plausible growth mechanism is proposed.

Zinc nitrate, on mixing with aqueous KOH solution, produce transparent zinc tetra hydroxide (zincket ion) and simultaneously zinc foil present in the same bottle, reacting with alkali, release zinc ion in the same solution following the reaction pathway:

$$Zn^{2+} + 4OH^{-} \rightarrow Zn(OH)_4^{2-} ,$$

$$Zn + 2H_2O + 2OH^{-} \rightarrow Zn(OH)_4^{2-} + H_2$$
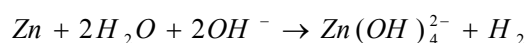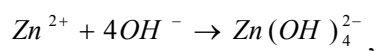
Continuous production of zincket ion in the solution via these pathways increase the super-saturation level; and once the critical limit required to overcome the nucleation energy barrier is crossed, ZnO nucleuses start to form homogeneously in solution as well as heterogeneously over the substrate which after maturing, form ZnO nanoform:

9

$$Zn(OH)_4^{2-} \rightarrow ZnO + H_2O + 2OH^-$$
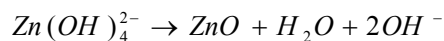
Wurtzite phase ZnO crystal is composed of stacked alternate polar planes of zinc (Zn^{2+}) and oxygen (O_2^-) ions where this peculiar stacking leads to difference in surface energies of crystal facets and ensued typical 1D growth of ZnO having the (002) plane at its top surface and non-polar planes as the side.

Additional to such preferential growth, diffusion rate of freshly prepared zincket ion from zinc foil also plays a critical role in longitudinal diameter controlling. Diffusion rate with comparable or higher value than the growth rate results 1D nanostructure with uniform diameter due to a homogenous growth environment. On the other hand; reverse circumstances create inhomogeneous growth surroundings for ingrowing 1D structure and result a negative gradient of precursors from base to tip. Such diameter shrinkage along length of the 1D structure consequently renders nanospike morphology.

For secondary branch growth, nucleation of new crystal over the existing/pristine nanoform is indispensible which take place spontaneously in the system in absence of any additional seeding protocols. Once nanospike coated substrate is introduced into similar sort of high alkaline solution, it encounters a harsh environment which etches the side surface of the nanospike.[47] As a consequence of such etching, the nanospike surfaces become rough and possibility of defect incorporation in these nanoform increases. It is experimentally confirmed that presence of such defect center serves as pin point for nucleation.[48] From these as formed nucleation sites, new secondary ZnO nanostructure start to cultivate after attaining the critical value, as discussed in the previous section. Small amount of zinc precursor in the solution deter the growth of secondary branches up to a limit and nanocactus morphology evolves. On the contrary, similar

10

experimental protocol except higher zinc nitrate concentration result higher dimensional nano branches over pristine nanospike.

Field emission:

Based on the general perception that nanostructures having high aspect ratio and sharp edges are propitious for high field emission performance, we have investigated the field emission characteristics of the synthesized samples. In general, ZnO nanospikes bestow high emission current as the emission performance is benefited by their sharp tip geometry and aspect ratio.[40] Therefore, geometrically modified nanospikes i.e. nanospikes armed with multiple sharp protruding branches is more likely to render an exalted FE performance, than the normal. Field emission current density (J) plot as a function of electric field strength (E) in Fig. 7a reveals remarkably enhanced emission current for the hierarchies in comparison to parent nanospike. ZnO nanospikes emit electrons with characteristic turn on (electric fields required for extracting an emission current of $10\mu A/cm^2$) of 3.01 which get downshifted to 2.03, and 1.44 $V\mu m^{-1}$ for nanotree and nanocactus respectively. The threshold field values (electric fields required for extracting an emission current of 1 mA/cm^2) for nanotree and nanocactus respectively are 5.09, 4.10 $V\mu m^{-1}$ respectively. However, the nanospike sample did not achieve the threshold value within the investigated range of electric field. Such low field values for the nanocactus sample are comparable or superior to the other inorganic semiconductor and thus signify its potential as efficient cold cathode. Field emission, electric field assisted electron extraction phenomenon from cathode to anode through quantum mechanical tunneling can be quantitatively explained on the basis of Fowler–Nordheim (F-N) equation according to which: $J = (A\beta^2 E^2 / \phi)\exp(-B\phi^{3/2} / \beta E)$. Here A and B are constants with values 1.56×10^{-10} ($AV^{-2}eV$) and 6.83×10^3 ($VeV^{-3/2}\mu m^{-1}$) respectively, $E = V/d$ (d is the anode-emitter

distance). "β" the geometrical field enhancement factor quantifying the electric field amplification ability of the emitter at the electron emitting site, were estimated from the slopes of the linear $\ln(J/E^2)$ vs. $1/E$ curves, known as F-N plot (presented in Fig. 7b). Linear nature of the F-N plot in high field region designates that the emission current originates due to barrier tunneling of electron. With the work function ($'\phi'$) taken to be 5.3 eV for ZnO estimated β values from the from their corresponding F–N plot were found to be 4473, 8771 and 14619 for nanospike, nanotree and nanocactus respectively.[49] Further, we have investigated the electron emission behavior of the nanocactus at different electrode separations within the range of 120–180 μm with an interval of 30 μm. With the increments of separation, the field values (turn on and the threshold field) values were downshifted very interestingly (Fig. 7c). For a facile comparative view, we tabulated all the field values in Table 1. Further, to check the figure of merit of our samples, we have compared them with different sorts of field emitters and tabulated them in Table S1† (Supporting information†).

Discernable differences in the field enhancement values among the synthesized products may account for several factors such as emitter tip geometry, number of emission sites, neighbor emitter cross-talking i.e. screening effect, crystallinity etc.[40,50] Emission favorable geometry i.e. the small radius of curvature for tip, good vertical alignment together with well crystallinity (evident from HRTEM and XRD) ensures moderate field emission performance from the nanospike. However in the nanospike, maximum electron emission takes place from their tip as smooth side surfaces lacks adequate emission sites which in turn impede the emission performance up to the mark. Now, as a consequence of surface decoration with protruding secondary branches, nanospike transform into nanocactus and nanotree shape and overall emission performance boosts up. Such increment can be enlightened with help of two parameters

namely; number of emission sites and geometrical arrangement. Appearance of numerous protruding branches with different degree of vertical orientation on smooth side surfaces of the nanospike ensue large number of emission site which impart an added advantage in electron emission.

Furthermore, this peculiar arrangement of branches over the nanospikes results in two stage field enhancement. For branched geometry, the applied primary field gets enhanced at the parent stems (ZnO nanospike) which in succession acts as effectively stronger applied bias at the base of branches and gets enhanced further.[50] Based on this analogy, the nanotree sample having larger number as well as higher aspect ratio emitters should exhibit highest field emission performance among all; however in practical scenario, it endows lower emission performance than the nanocactus. In nanotree sample, inter emitter closed proximity driven high field screening impede electron emission and produces a relatively low performance due to emission beneficial features aspect getting overshadowed by the negative influence of the screening as it has exponential dependence over emitter separation.[51] Therefore, on the basis of screening, the emission current corresponding to nanospikes should have been maximum; however the registered converse behavior confirms the dominance of adverse effect of low emission sites over screening. Lastly, nanocactus with optimal emitter density along with sizable inter-emitter separation compensates the detrimental influence of screening, and thereby offers best performance. Furthermore, oxygen vacancy concentration has significant impact on electron emission which was pointed out in our previous work.[43] Surface defects such as oxygen vacancies acting as adsorption sites create an additional surface potential barrier for the electrons and for greater number of vacancy constitution, potential barrier height becomes higher. Thus nanotree sample with higher oxygen vacancy than the nanocactus (obvious from CL spectra)

13

exhibits relatively lower characteristic field values than the latter. Finally, the anode-emitter separation dependent field emission behavior as observed in our case is consistent with previous reports.[12,52] With increased electrode distance, the effective emission area increases, and a greater number of electrons can reach the collector, which results in increased current density.[53]

Besides high emission current at lower electric field, temporal stability of emission currents for long time duration is also another decisive criterion of a practical electron emitter. To address this issue we have investigated the temporal variation of the field emission current with initial emission current density 1 mA/cm^2 for all synthesized samples (Fig. 7d). The assessed fluctuations values in the emission currents for nanospike, nanocactus and nanotree are 12%, 9%, and 3% respectively. Nominal fluctuation as well as no signature of current degradation with time suggests the highest electron emission stability of the nanotree sample. Such stability of the nanotree can be attributed to their high surface area thereby larger radiation area and lower resistance, which ease the heat dissipation procedure.[54]

Theoretical correlation:

In order to verify our experimental field electron emission results, we have used a finite element method (ANSYS Maxwell simulation package) to investigate the local electric field distribution of the as synthesized samples. Initially, we designed 3D models of these nanostructures and chosen the simulation keys in such fashion that it can easily replicate the as synthesized morphology and make the simulation simple. Nevertheless, configurations of the models were based on the typical morphology and dimension of three types of nanoforms in our experiments. For nanospike sample, we consider a single nanospike with smooth side surfaces having length ~250 nm and a diameter that changes from ~50 nm to 10 nm from base to top whereas for nanocactus we decorate the parent nanospike surface with sparsely distributed low aspect ratio

14

secondary branches having average length ~ 50 nm and diameter ~ 30 nm to 10 nm base to top. Further, for nanotree sample, number density of secondary branches as well as their dimension is also increased. During the simulation, the inter electrode separation (~180 μm), dielectric constant (ε_{ZnO} = 8.66),[55] applied electric field (F_M = 2.2 kV), type of the collector and etc. are maintained as actual experimental parameters in all stimulation. A rainbow colored coordinate in Fig. 8 represents the different electric field intestines where the red and blue colors indicate maximum and minimum field values respectively. Predominant confinement of the local electric field at the top of the nanospike and nanotree is obvious from the figure which restricts their emission performance. On the contrary, the field emission distribution throughout the whole nanostructure surfaces offers highest electron emission for the nanocactus sample which is also prominent from the figure. Considering the presence of inter emitter cross talking, one can easily envisage inferior emission performance in nanotree than the nanocactus sample and the analogues result also manifests from the simulation. Though its performance was hampered to some extent by the screening of adjacent emitter, yet at the same time presence of higher number of emitter also beneficiated the emission. Such reasoning with high number of emission site can explain the performance difference between nanotree and nanospike. Maximum field values from the model was found to be 1.96×10^7 (F_1), 5.10×10^7 (F_2) and 2.75×10^7 (F_3) for nanospike, nanocactus and nanotree respectively. Field enhancement factors (β) for these samples can be calculated by taking the ratio of maximum field to the applied electric field i.e. ($\beta = F_1 / F_M$). As in all cases the applied electric field are same, thus the ratio of β is same as the ratio of the maximum electric field and which is found to be 1: 3.26: 1.96 for nanospike, nanocactus and nanotree respectively. Thus the simulated results predict the highest enhancement factor of nanocactus and nominal for nanospike which is in well agreement with our experimental results.

15

Fig.9 illustrate 3-dimensional simulated electric field distribution results based on the cactus model for different anode-emitter separations where $d = 120, 150, 180$ μm respectively. From the color plots, the highest field emission current distribution for largest vacuum gap is very prominent which also upholds our experimental results.

UV response:

Semiconductor nanostructures have already registered their supremacy as efficient UV detectors,[56] which are supposed to originate from their high specific surface area and uniquely designed surfaces as it ensured enhanced interaction probability of light-matter with the nanostructure surface.[57,58] In this aspect, nano-tree architecture have the propitious to be a competent candidate for UV light detection as it possesses highest surface area in comparison to other synthesized nanoforms (clear from BET results). The schematic of photocurrent measurement configuration using two probe contacts (Fig. 10a) and linear current voltage (I-V) characteristics of the nanospike sample measured at completely dark and UV illumination are shown in Fig. 10b. Such linear I-V dependence signifies an ohmic nature of the junction with deposited top gold electrodes. Prior to electrical measurement, all the samples were kept in complete darkness for few hours to attain equilibrium condition. Photocurrent growth and decay of the fabricated detectors measured in air ambient at a fixed bias of 2V in response to UV light (350 nm) ON and OFF are presented in Fig. 10c. These transient response curves indicate high UV sensitivity of samples as before UV irradiation, dark current (I_d) were 9.91×10^{-9}, 4.57×10^{-9} and 1.63×10^{-10}A and on illumination large changes in currents resulted where the elevated values were found to be 3.26×10^{-7}, 1.12×10^{-6}, 3.61×10^{-6} A for nanospike, nano-cactus and nano-tree respectively. Photocurrent gain (η) defined as ratio of total photocurrent $(I_{ph} + I_d)$ to dark current (I_d) is only 3.38×10^{1} for nanospike while the same was enhanced by an order of magnitude to $\sim$

16

2.46×10^2 for nanocactus and further improved to 2.21×10^4 for nanotree. Additionally, photocurrent growth and decay times (times taken for the increase of photocurrent by one order of magnitude after UV ON and decrease by one order after UV OFF), estimated from the curves confirm the fastest UV response for nanospike and reverse for nanotree samples. Photocurrent switching behavior at same bias voltage (2V) was accessed as a function of time via periodic turning on and off the UV source and presented in Fig. 10d which further signifies the excellent reproducibility and stability of the device. Very high decay time for the nanotree sample as compared to others is very obvious form the same figure. Even 10 min after UV light off, it did not come back to its initial dark value and so at the beginning of next cycles still there are some residual current i.e. the next cycles start from a slightly high dark current value. Progressively increasing I_d value in the consecutive cycle's resulted in higher total photocurrent ($I_{ph}+ I_d$) in any cycle as compared to previous one. Finally for a facile comparative view, all the UV parameters for as synthesized samples were tabulated in Table 2 which indicates the response supremacy for nanotree sample and the vice versa for nanospike sample. Further, a comparison is made in Table S2† (supporting information†) with respect to dark current, photocurrent and gain values of our sample with previously reported ones to enlighten its importance in UV detection.

Prior to detailed enlightenment on the basis owing to which such noticeable differences in photoconduction behavior of the synthesized samples were resulted, depth understanding of the photo-detection mechanism in ZnO is very essential.

In dark, physisorbed and chemisorbed oxygen (O_2) molecules over ZnO surfaces, through free electron killing in conduction band, get ionized to O_2^- following the equation $O_2 + e^- = O_2^-$. Further, simultaneous formation of depletion layer by forming an upward band bending decreases the mobility of the rest of the carriers.[56] Consequence of these two factors overall

reduced dark conductivity of zinc oxide is resulted. Upon UV exposure (energy greater than or comparable with the band gap of ZnO), photo-excited electron–hole pairs are generated ($h\nu = e^-$ $+ h^+$). Following the as formed potential inclination, photo-excited holes transfer towards the nanostructure surface and trapped by negatively charged oxygen ions through surface electron–hole recombination.[56] On the other hand, photo-generated unpaired electrons with increased lifetime remain in conduction band which in turn significantly increases the conductivity. Finally again in OFF condition, the O_2 molecules re-adsorb on the nanostructure surface until current restores to the dark value.[56]

A schematic of UV detection mechanism in ZnO nanostructures in at dark condition and under UV illumination is presented in Fig. 10d. Further the schematic of the band diagram of the same phenomenon under dark and illumination is also displayed in Fig. 10(e,f). As mentioned above, in dark, surface states by capturing free electrons determines the current, thus nanostructures having highest surface area should exhibit the lowest dark current due to highest carrier annihilation. Further the high active surface area of the nanostructures felicitates light matter interaction more; thereby the carrier generation is to be expected highest in these materials. From the BET results (Fig. 4), maximum and minimum surface area corresponds to nanotree and parent nanospike respectively is very much obvious i.e. the surface area of the nanostructure followed the order: nanospike < nanocactus < nanotree. So the dark current and photocurrent gain should follow the analogous order as both are mainly originated due to the variation in surface area. Additionally in ZnO, the oxygen vacancy related surface defect behaving as the donor increases the carrier concentration.[56,59] Owing to highest defect constitution (clear from CL spectra) the nanotree sample should exhibit highest gain compared to others. Such explanations with structural parameters as well as intrinsic defect structure behind the variation

of photocurrent gain and dark current are consistent with the observed result. Finally the difference on transient response time can be accounted for by the variation in defect and generally nanostructure with utmost defect concentration exhibited high growth and decay time which also corroborate the observed.

Conclusion:

In summary, a zero thermal budget, rationally developed eco-friendly approach is undertaken to generate zinc oxide hierarchical nanoform nanowires in large scale. Starting with 1D nanospike array, higher dimensional nanoforms with different geometrical complexity is realized where the nucleation for secondary branch evolution and subsequent growth occur in the same reaction. Absences of post growth high temperature modification steps as well as large area fabrication capability are the hallmarks of this protocol. A comparative study revealed highest field electron emission ability of the nanocactus sample and suggested it to be the fittest candidate for designing cold cathode based devices among all. From the photodetection perspective, nanotree sample emerged to be the best one as a consequence of morphological as well as defect enriched features. This work will open up a new direction to integrate a new catalogue of hierarchical architecture in subtle manner and thereby would facilitate their usages in several types of nanoscale electronic and optoelectronic devices.

Acknowledgement:

Reference:

(1)   H. Kim, S. Jeon, M. Lee, J. Lee and K. Yong, *J. Mater. Chem.,* 2011, **21**, 13458.

(2)   H. Jung, S. H. Lee, J. Yang, M. Cho and Y. Lee, *RSC Adv.,* 2014, **4**, 7714.

(3)   U. K. Gautam, M. Imura, C. S. Rout, Y. Bando, X. Fang, B. Dierre, L. Sakharov, A. Govindaraj, T. Sekiguchi, D. Golberg and C. N. R. Rao, *PNAS*, **107,** 13588.

(4)   L. Xu, Q. Chen and D. Xu, *J. Phys. Chem. C,* 2007, **111**, 11560.

(5)   C. Gu, C. Cheng, H. Huang, T. Wong, N. Wang and T.-Y. Zhang, *Cryst. Growth Des,* 2009, **9**, 3278.

(6)   F. Zhao, J.-G. Zheng, X. Yang, X. Li, J. Wang, F. Zhao, K. S. Wong, C. Liang and M. Wu, *Nanoscale*, 2010, **2,** 1674.

(7)   H. Sun, Y. Yu, J. Luo, M. Ahmad and J. Zhu, *CrystEngComm,* 2012, **14**, 8626.

(8)   S. Pal, S. Maiti, U. N. Maiti and K. K. Chattopadhyay, *CrystEngComm,* 2015, **17**, 1464.

(9)   M. R. Alenezi, A. S. Alshammari, T. H. Alzanki, P. Jarowski, S. J. Henley and S. R. P. Silva, *Langmuir,* 2014, **30**, 3913.

(10)   Y. Zhang, J. Xu, Q. Xiang, H. Li, Q. Pan and P. Xu, *J. Phys. Chem. C,* 2009, **113**, 3430.

(11)   C. Park, H.-M. So, H. J. Jeong, M. S. Jeong, E. Chang, W. S. Pippel and S.-M. Lee, *ACS Appl. Mater. Interfaces,* 2014, **6**, 16243.

(12)   S. Pal, S. Maiti, U. N. Maiti and K. K. Chattopadhyay, *J. Mater. Chem. C,* 2014, **2**, 4005.

(13)   S. S. Warule, N. S. Chaudhari, R. T. Khare, J. D. Ambekar, B. B. Kalea and M. A. More, *CrystEngComm,* 2013, **15**, 7475.

(14) F. Xu, J. Chen, Y. Di, Y. Cui, J. Sun, L. Sun, W. Lei, C. Xu and W. Zhou, *RSC Adv.*, 2012, **2,** 11601.

(15) U. K. Gautam, L. S. Panchakarla, B. Dierre, X. Fang, Y. Bando, T. Sekiguchi, A. Govindaraj, D. Golberg and C. N. R. Rao, *Adv. Funct. Mater.*, 2009,**19,** 131.

(16) M. Raja, N. Muthukumarasamy, D. Velauthapillai, R. Balasundaraprabhu, S. Agilan and T. S. Senthil, *Sol. Energy,* 2014, **106**, 129.

(17) D. Wu, Z. Gao, F. Xu, J. Chang, W. Tao, J. He, S. Gao and K. Jiang, *CrystEngComm,* 2013, **15**, 1210.

(18) H. Kim and K. Yong, *Phys. Chem. Chem. Phys.,* 2013, **15**, 2109.

(19) S. Garry, É. McCarthy, J.-P. Mosnier and E. McGlynn, *Nanotechnology,* 2014, **25**, 135604.

(20) S. Singh, K. C. Barick and D. Bahadur, *CrystEngComm,* 2013, **15**, 4631.

(21) P. Wang, X. Zhang, J. Wen, L. Wu, H. Gao, E. Zhang and G. Miao, *J. Alloys Compd.,* 2012, **533**, 88.

(22)   Z. Wang, J. Gong, Y. Su, Y. Jiang and S. Yang, *Cryst. Growth Des.,* 2010, **10**, 2455.

(23) C.-L. Hsu and S.-J. Chang, *Small*, 2014, **10,** 4562.

(24) M. Klaumünzer, M. Distaso, J. Hübner, M. Mačković, E. Spiecker, C. Kryschi and W. Peukert, *CrystEngComm,* 2014, **16**, 1502.

(25)   H. Zhang, R. Wu, Z. Chen, G. Liu, Z. Zhang and Z. Jiao, *CrystEngComm,* 2012, **14**, 1775.

(26)   L. Xu, Z. Li, Q. Cai, H. Wang, H. Gao, W. Lv and J. Liu, *CrystEngComm,* 2010, **12**, 2166.

(27)   Q.-P. Luo, B.-X. Lei, X.-Y. Yu, D.-B. Kuang and C.-Y. Su, *J. Mater. Chem.,* 2011, **21**, 8709.

(28)   F. Xu, Y. Shen, L. Sun, H. Zeng and Y. Lu, *Nanoscale,* 2011, **3**, 5020.

(29)   Y. Chang, Y. Lu, M. Wang, Y. Long and R. Ye, *Appl. Surf. Sci.,* 2013, **264**, 687.

(30)   F. Xu, M. Dai, Y. Lu and L. Sun, *J. Phys. Chem. C,* 2010, **114**, 2776.

(31)   C.-T. Wu and J.-J. Wu, *J. Mater. Chem.* 2011, **21**, 13605.

(32)   R. F. Zhuo, H. T. Feng, J. T. Chen, D. Yan, J. J. Feng, H. J. Li, B. S. Geng, S. Cheng, X. Y. Xu and P. X. Yan, *J. Phys. Chem. C,* 2008, **112**, 11767.

(33)   K.-M. Kim, H.-R. Kim, K.-I. Choi, H.-J. Kim and J.-H. Lee, *Sens. Actuators, B,* 2011, **155**, 745.

(34)   Z. Han, L. Liao, Y. Wu, H. Pan, S. Shen and J. Chen, *J. Hazard. Mater.,* 2012, *217*, 100.

(35)   S. H. Ko, D. Lee, H. W. Kang, K. H. Nam, J. Y. Yeo, S. J. Hong, C. P. Grigoropoulos and H. J. Sung, *Nano Lett.,* 2011, **11**, 666.

(36)   U. N. Maiti, S. Maiti and K. K. Chattopadhyay, *CrystEngComm,* 2012, **14**, 640.

(37) Z. Pan, P. Zhang, X. Tian, G. Cheng, Y. Xie, H. Zhang, X. Zeng, C. Xiao, G. Hu and Z. Wei, *J. Alloys Compd.,* 2013, **576**, 31.

(38) R. Al-Gaashani, S. Radiman, A. R. Daud, N. Tabet and Y. Al-Douri, *Ceram. Int.,* 2013, **39**, 2283.

(39) D. K. Kim and H. B. Kim, *J. Alloys Compd.,* 2011, **509**, 421.

(40) U. N. Maiti, S. Maiti, S. Goswami, D. Sarkar and K. K. Chattopadhyay, *CrystEngComm,* 2011, **13**, 1976.

(41) O. Lupan, L. Chow, G. Chai, B. Roldan, A. Naitabdi, A. Schulte and H. Heinrich, *J. Mater. Sci. Eng. B,* 2007, **145**, 57.

(42) H. Liu, L. Hu, K. Watanabe, X. Hu, B. Dierre, B. Kim, T. Sekiguchi and X. Fang, *Adv. Funct. Mater.,* 2013, **23,** 3701.

(43) S. Maiti, U. N. Maiti, B. C. Behera, S. Pal and K. K. Chattopadhyay, *J. Mater. Chem. C,* 2013, **1***,* 4940.

(44) U. N. Maiti, S. Maiti, R. Thapa and K. K. Chattopadhyay, *Nanotechnology,* 2010, **21**, 505701.

(45) A. Umar, S. H. Kim, Y.-S. Lee, K.S. Nahm and Y. B. Hahn, *Cryst. Growth Des.,* 2005, **282**, 131.

(46) P. Ma, Y. Wu, Z. Fu and W. Wang, *Adv. Powder Technol.,* 2012, **23**, 170.

(47) J. Wu and D. Xue, *Mater. Res. Bull.,* 2010, **45**, 295.

(48)   Y. Tong, Y. Liu, L. Dong, D. Zhao, J. Zhang, Y. Lu, D. Shen and X. Fan, *J. Phys. Chem. B,* 2006, **110**, 20263.

(49)   U. N. Maiti, S. Maiti, T. P. Majumder and K. K. Chattopadhyay, *Nanotechnology,* 2011, **22**, 505703.

(50)   U. K. Gautam, X. Fang, Y. Bando, J. Zhan and D. Golberg, *ACS Nano,* 2008, **2**, 1015.

(51)   S. Maiti, U. N. Maiti, S. Pal and K. K. Chattopadhyay, *Nanotechnology,* 2013, **24**, 465601.

(52)   A. Khademi, R. Azimirad, A. A. Zavarian and A. Z. Moshfegh, *J. Phys. Chem. C,* 2009, **113**, 19298.

(53)   A. N. Banerjee and S. W. Joo, *Nanotechnology,* 2011, **22**, 365705.

(54)   P. Feng, X. Q. Fu, S. Q. Li, Y. G. Wang and T. H. Wang, *Nanotechnology,* 2007, **18**, 165704.

(55)   Y. Yang, W. Guo, X. Wang, Z. Wang, J. Qi and Y.Zhang, *Nano Lett.,* 2012, **12**, 1919.

(56)   U. N. Maiti, K. K. Chattopadhyay, S. Karan and B. Mallik, *Scr. Mater.,* 2010, **62**, 305.

(57)   L. Peng, L. Hu and X. Fang, *Adv. Mater.*, 2013, **25,** 5321.

(58)   H. Liu, Z. Zhang, L. Hu, N. Gao, L. Sang , M. Liao, R. Ma, F. Xu, and X. Fang, *Adv. Optical Mater.*, 2014, **2,** 771.

(59)   M. Dutta, S. Mridha and D. Basak, *Appl. Surf. Sci.,* 2008, **254**, 2743.

 Figure caption:
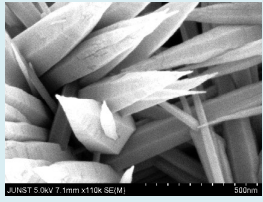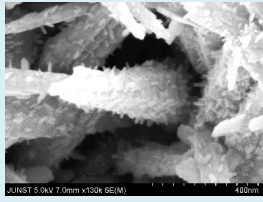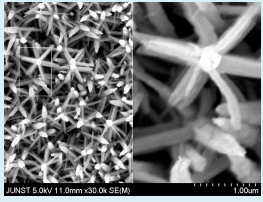
(1)   FESEM images of the synthesized ZnO [a,b] nanospike (low and high magnification) (c) nanocactus (d) nanotree; inset shows the wafer scale synthesis.

(2)   TEM, HRTEM images and corresponding SAED patterns of the synthesized samples.

(3)   (a) XRD patterns of the synthesized products; XPS spectrum of (b) O 1s, (c) Zn 2p, and (d) survey for nanotree.

(4) N_2 gas adsorption-desorption isotherm of ZnO (a) nanospike, (b) nanocactus and (c) nanotree.

(5)   (a) Room temperature CL spectra, (b) EDX spectra and atomic weight percentage and (c) Raman spectra for the synthesized samples.

(6)   Schematic illustrating the synthesis procedure of ZnO nanospike to hierarchy formation on glass/ ITO coated glass substrate.

(7)   (a) J–E plots and (b) corresponding F–N plots for the samples under investigation; (c) J–E plots of nanocactus sample with different vacuum gaps; (d) emission stability for all samples.

(8)   Computed results along with color mapping of magnitude of electric field distribution as overlay for (a) nanospike; (b) nanocactus and (c) nanotree.

(9)   Three dimensional perspective of ZnO nanocactus along with computed electric field distribution as overlay at (a) 120, (b) 150 and (c) 180 μm anode-emitter separations.

(10)   (a) Schematic of the photoconductivity measurement setup, (b) I–V characteristics of the samples in dark, (c) Plot of the growth and decay of photocurrent measured with 350 nm

25

UV excitation as the UV light for all samples; (d) Photoresponse cycles of all samples, (e) schematic of the UV detection mechanism of ZnO nanostructure and (f) band diagram for dark and illuminated condition.

Table 1: FE Parameters of the Synthesized ZnO Samples

FE PARAMETERS	NANOSPIKE	NANOCACTUS	NANOTREE
Turn on field (V/μm)	3.01	1.44	2.03
Threshold field (V/μm)	….	4.10	5.09
β value	4473	14619	8771

Table 2: BET Surface Area Value and UV Detector Parameters of synthesized ZnO Samples

PROPERTY	NANOSPIKE	NANOCACTUS	NANOTREE
BET surface area (m^2/g)	34.461	49.856	68.576
Dark current (A)	9.91×10^{-9}	4.57×10^{-9}	1.63×10^{-10}
Photo current (A)	3.26×10^{-7}	1.12×10^{-6}	3.61×10^{-6}
Photocurrent gain (η)	3.38×10^{1}	2.46×10^{2}	2.21×10^{4}
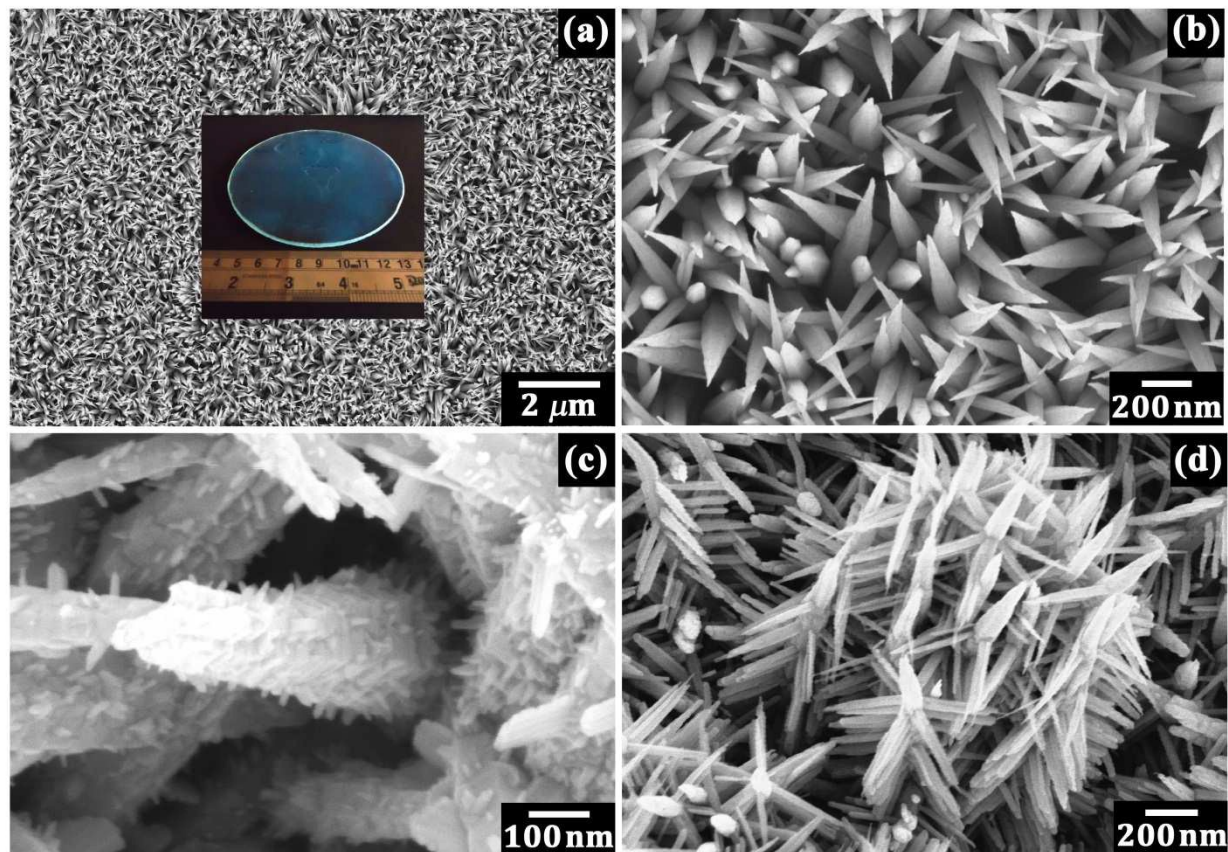
Fig.1 Pal et al.
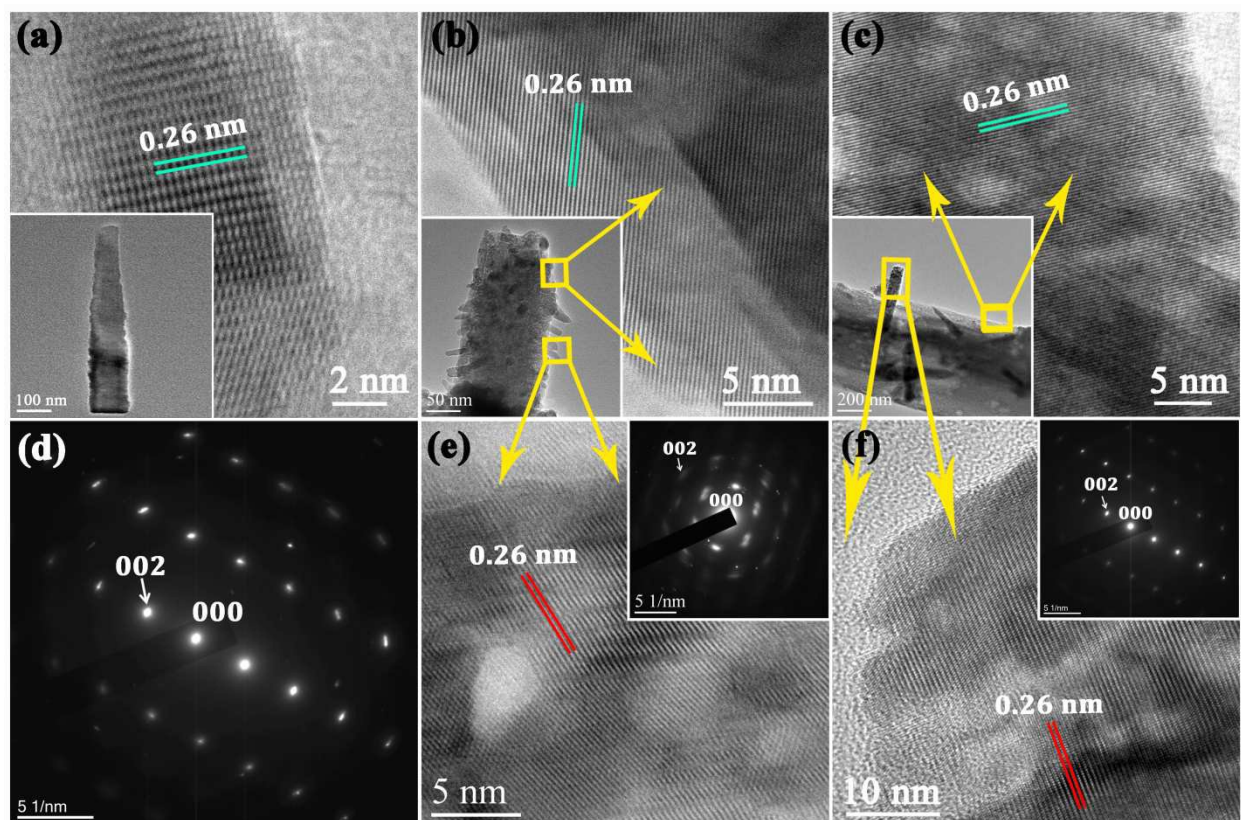
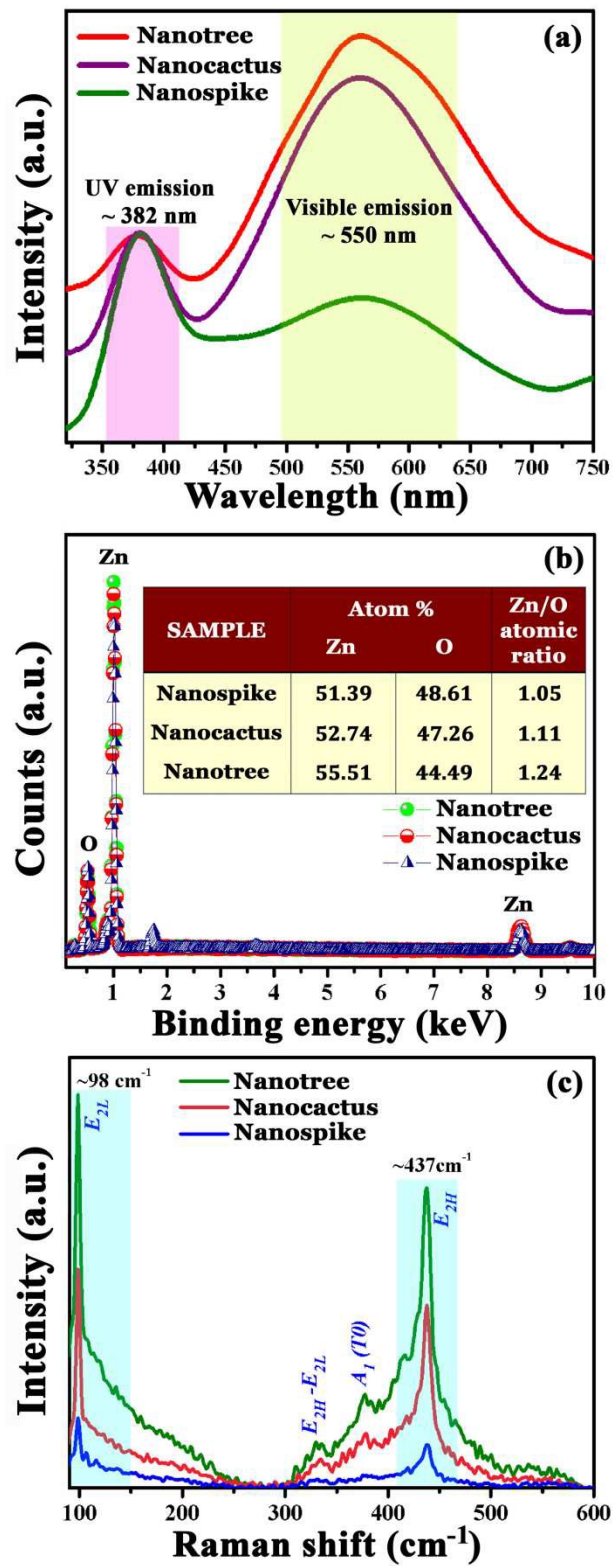**Fig.2 Pal et al.**
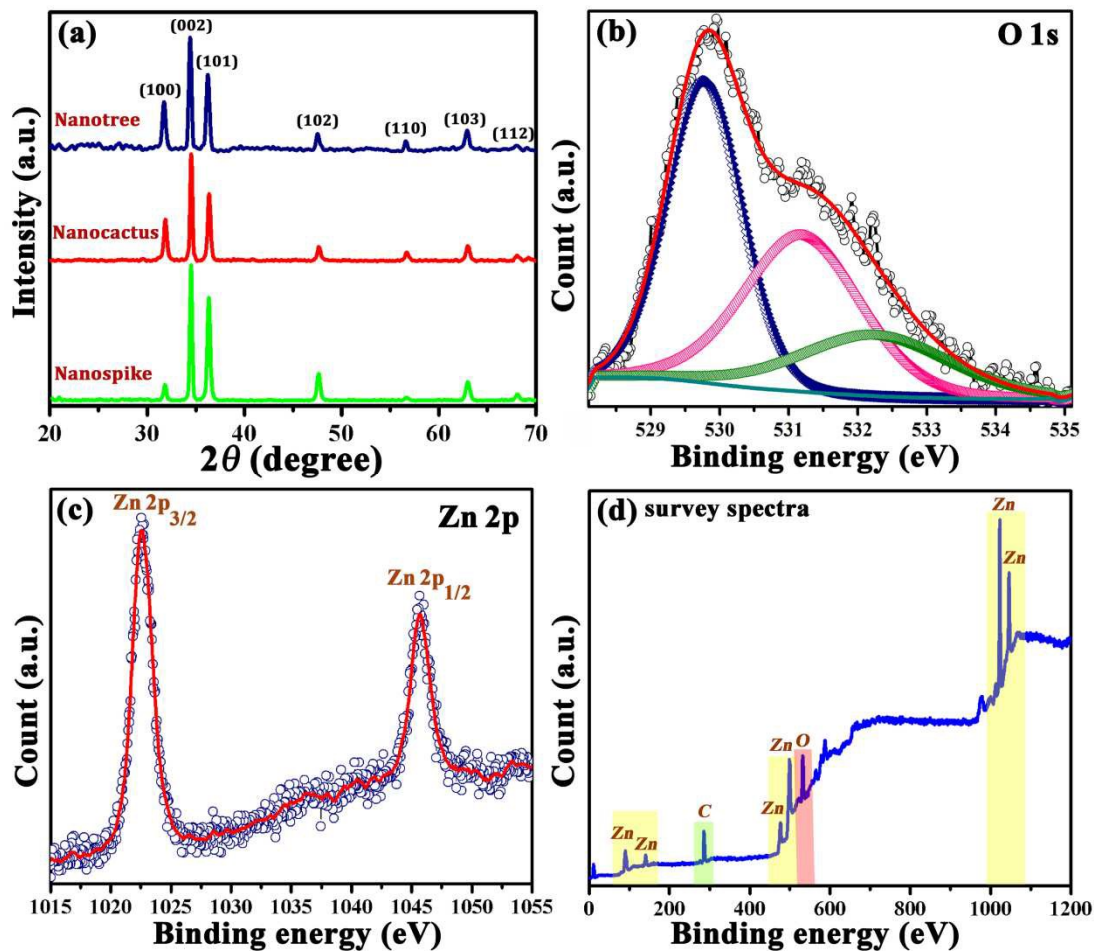
Fig.3 Pal et al.

Fig.4 Pal et al.

29
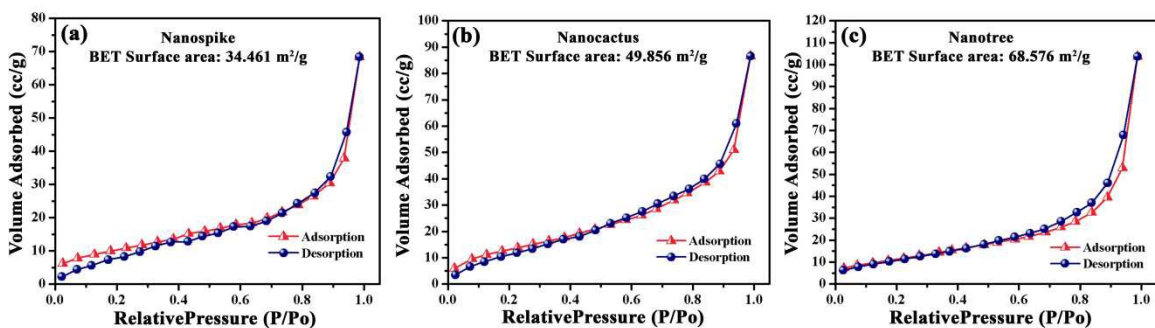
Fig.5 Pal et al.
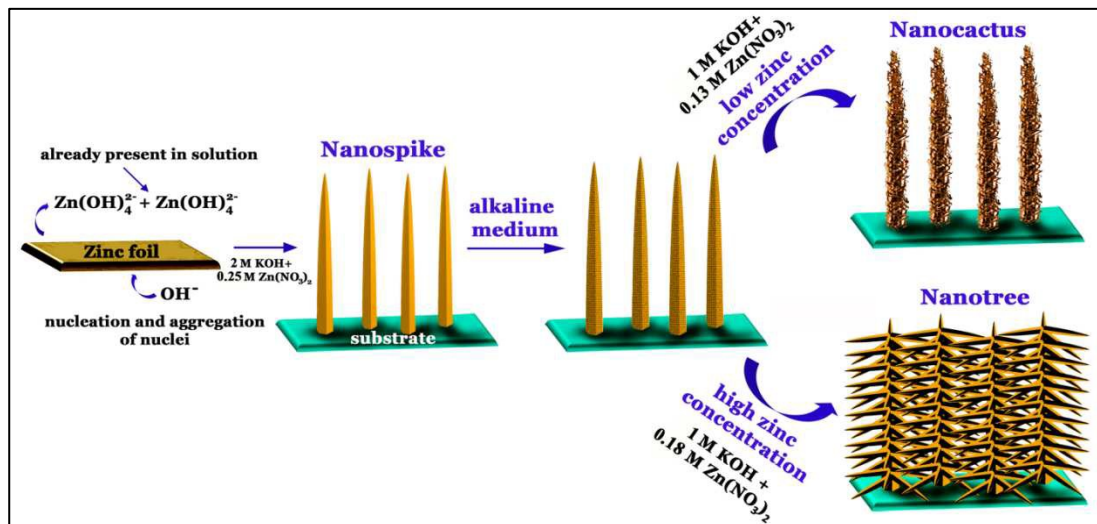
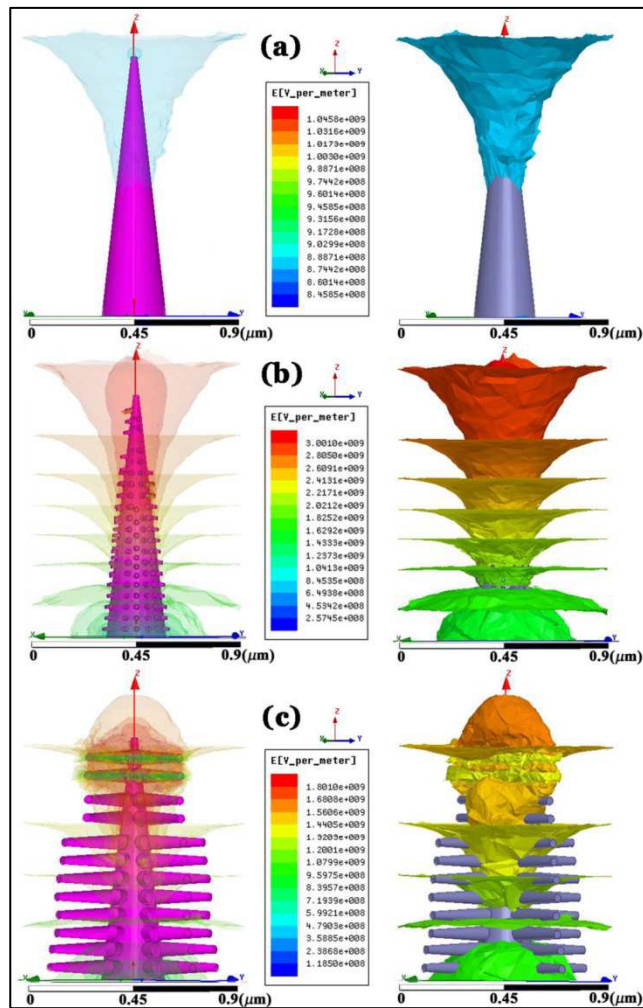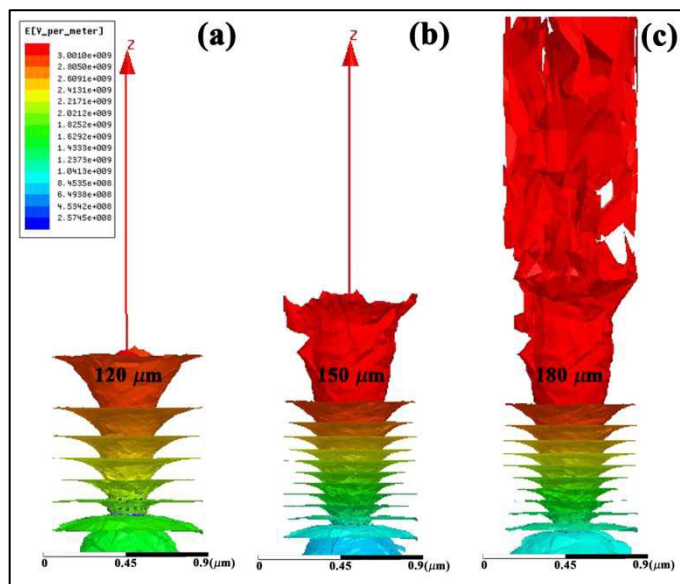**Fig.6 Pal et al.**
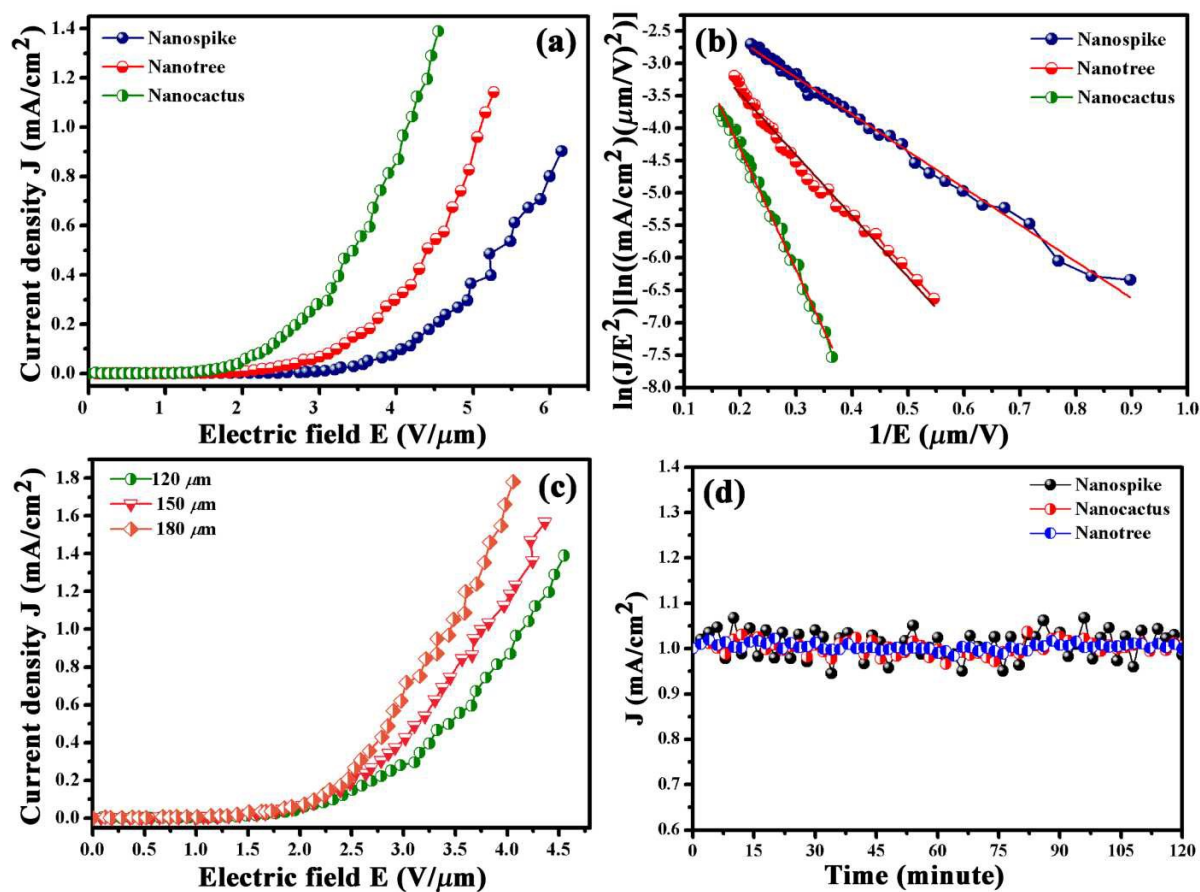
Fig.7 Pal et al.

Fig.8 Pal et al.

Fig.9 Pal et al.

Fig.10 Pal et al.